International Journal of Heat and Mass Transfer 80 (2015) 789–801

Contents lists available at ScienceDirect

International Journal of Heat and Mass Transfer

journal homepage: www.elsevier.com/locate/ijhmt

Analysis of collimated irradiation under local thermal non-equilibrium condition in a packed bed

P. Wang [a,b], K. Vafai [b,*], D.Y. Liu [a], C. Xu [a]

[a] Department of Renewable Energy Science and Engineering, Hohai University, Nanjing, China
[b] Department of Mechanical Engineering, University of California, Riverside, USA

ARTICLE INFO

Article history:
Received 16 July 2014
Received in revised form 9 September 2014
Accepted 10 September 2014

Keywords:
Porous media
Local thermal non-equilibrium
Convective heat transfer
Collimated irradiation
Modified differential approximation (P-1)

ABSTRACT

Forced convective heat transfer in a packed bed in the presence of collimated irradiation and under local thermal non-equilibrium is analyzed in this work. Both the collimated and diffusive radiative transfer processes are accounted for using the modified P-1 approximation. Two boundary condition models considering different limiting conditions at the wall which couple radiation and convection under LTNE were constructed. The effect of pertinent parameters such as the porosity φ, pore diameter d_p, ratio of the solid to fluid thermal conductivities ζ; radiative properties including optical thickness τ, scattering albedo ω, and the wall emittance ε_w were analyzed. Also, their effects on the temperature and heat flux distributions in the incident direction were analyzed systematically and the limiting interactions between thermal radiation and conduction were revealed. The differences between the two boundary models with the effects of the cited parameters were analyzed. Our analysis demonstrated that an increase in either φ or d_p enhances the transfer of radiative energy into the channel.

1. Introduction

Porous media is widely used in many modern industrial applications due to its excellent attributes, such as high thermal conductivity, large specific area and high resistant to heat shock. Many research works have been carried out investigating the use of porous media in various applications such as solar thermal energy, nuclear waste storage, heat pipes and heat transfer enhancement [1]. The local thermal non-equilibrium (LTNE) model describes the heat transfer process in a porous medium [2,3]. Variants of this model was given by B. Alazmi and K. Vafai [4] considering the effect of non-Darcy, dispersion, non-equilibrium and variable porosity. The effect of different boundary conditions under LTNE conditions was given by Yang and Vafai [5,6]. For high temperature cases, thermal radiation behavior cannot be neglected [7–9]. Its impact on conductive heat transfer in a packed bed has been analyzed by Singh and Kaviany [10,11]. For an open-cell structure porous medium, Zhao et al. [12,13] investigated the radiation properties of an ideal structure analytically. The radiative properties such as spectral volumetric absorption and scattering coefficients of porous structures have been obtained experimentally by Hendricks and Howell [14,15] and Baillis et al. [16,17]. Wang et al. [18] have studied the influence of the radiation transfer on coupled heat transfer process with conduction and convection in a porous medium for a typical industrial device. Flamant and Olalde [19] have investigated the radiation transfer process in a double layer structure (glass bed and SiC porous layer) experimentally using a two-flux approximation to obtain the temperature distribution. Using the same method, Skocypec et al. [20] analyzed the model for oxidized wires in an air receiver; which compared quite well with the experimental result of Chavez and Chaza [21]. The heat transfer characteristics of this type of a porous medium was also numerically analyzed by Bai [22] and Xu et al. [23] and later validated by Wu et al. [24] considering different operational conditions.

Not much attention has been devoted to the effect of the collimated incident radiation in a two dimensional channel. For such a situation, the distribution of radiative energy changes in the incident direction and should be taken into account simultaneously with the convective processes. The purpose of the current study is to understand the role of the collimated incident radiation on the convective heat transfer in a porous channel under LTNE conditions. In this work, the temperature fields for the solid matrix and fluid phases will be analyzed while incorporating the local thermal non-equilibrium along with the modified differential approximation (P-1 model). The corresponding boundary conditions coupling radiation with conduction under LTNE condition will be established and the effect of intrinsic properties including

* Corresponding author.

http://dx.doi.org/10.1016/j.ijheatmasstransfer.2014.09.021
0017-9310/

Nomenclature

c_p	specific heat of fluid at constant pressure (J kg^{-1} K^{-1})
d_p	pore diameter (m)
F	empirical function
G	incident radiation
H	height of the porous channel
H_c	the remnant collimated radiative flux arriving at the bottom wall
h_{sf}	fluid-to-solid heat transfer coefficient (W m^{-2} K)
K	permeability (m^2)
L	length of a porous channel
Nu	Nusselt number
P	pressure (Pa)
Pr	Prandtl number
q_0	initial impinging heat flux at the upper wall
q_{in}	initial heat flux (W/m^{-2})
q	heat flux
Re_d	pore Reynolds number
T	temperature (K)
u	velocity (m/s)
$\boldsymbol{V}$	velocity vector (m s^{-1})
$\boldsymbol{x}$	spatial coordinate, horizontal
$\boldsymbol{X}$	dimensionless x
$\boldsymbol{y}$	spatial coordinate, vertical
$\boldsymbol{Y}$	dimensionless y

Greek symbols

α_{sf}	specific surface area of a porous medium (m^{-1})
β	extinction coefficient (m^{-1})
ε	emissivity
φ	porosity
$\boldsymbol{\Phi}$	example quantity
κ	absorption coefficient
λ	thermal conductivity (W m^{-1} K^{-1})
μ	dynamic viscosity (kg m^{-1} s^{-1})
σ	Stefan–Boltzmann constant
σ_s	scattering coefficient
γ	heat flux distribution parameter
θ	dimensionless temperature
ζ	ratio of solid to fluid thermal conductivities
ρ	density (kg m^{-3})
τ	optical thickness
τ_H	optical thickness at the position $y = 0$
ω	single scattering albedo
$\boldsymbol{\Psi}$	dimensionless radiative flux

Subscripts

a	average
c	collimated
d	Diffuse
e	effective/environment
f	fluid phase
m	mean value
r	radiative
s	solid phase
t	total
w	wall

some key optic parameters will be discussed. In addition the difference between the two boundary condition models will be discussed. Finally, the effect a wide range of variations in the governing parameters such as the porosity, φ, and the pore diameter, d_p on the heat transfer process will be systematically analyzed.

2. Model description

2.1. Physical model and assumptions

A fundamental configuration composed of a parallel plate channel filled with a porous medium as shown in Fig. 1 is considered. The computational area has the height H and the length L. The extension in the z direction is assumed to be long enough so that the problem will be essentially a two dimensional configuration. The inlet velocity at the entrance is uniform and the imposed constant heat flux is considered to be the collimated irradiation impinging perpendicularly on the upper wall. The heat transfer process in the incident direction will be analyzed based on the following assumptions:

1. The upper wall of channel is treated as transparent to the collimated irradiation but opaque and adiabatic for the inner radiation.
2. The upper and bottom walls are taken to be diffuse-gray surfaces with a negligible thickness.
3. The radiation transfer between the entrance and outlet surface and the upper and bottom walls is negligible.
4. The flow is steady and incompressible.
5. The thermophysical properties including the radiative properties of the fluid and the porous matrix are assumed to be isotropic, homogeneous and constant.

2.2. Mathematical model

2.2.1. Governing equations [2–9]

Conservation of mass:

$$\nabla \cdot \langle \boldsymbol{V} \rangle = 0 \tag{1}$$

Momentum equation:

$$\frac{\rho_f}{\varphi}\langle(\boldsymbol{V}\cdot\nabla)\boldsymbol{V}\rangle = \frac{\mu_f}{\varphi}\nabla^2\langle \boldsymbol{V}\rangle - \nabla\langle P\rangle^f - \frac{\mu_f}{K}\langle \boldsymbol{V}\rangle - \frac{\rho_f F\varphi}{\sqrt{K}}[\langle \boldsymbol{V}\rangle\cdot\langle \boldsymbol{V}\rangle]\boldsymbol{J} \tag{2}$$

where K is the permeability and the empirical function F depends primarily on the microstructure of the porous medium and can be represented as:

$$K = \frac{\varphi^3 d_p^2}{150(1-\varphi)^2} \tag{3}$$

$$F = \frac{1.75}{\sqrt{150\varphi^{3/2}}} \tag{4}$$

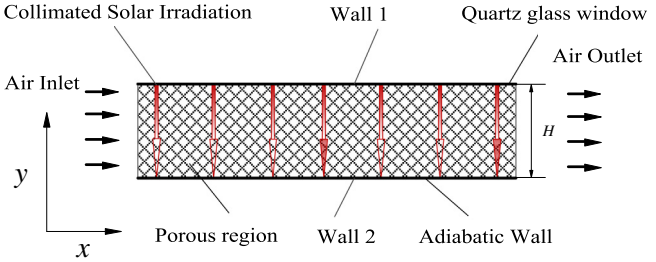

Fig. 1. Schematic diagram of the problem and the corresponding coordinate system.

where $\langle P\rangle^{f}$ is the gauge pressure and the local volume average of a quantity Φ can be defined as $\langle\Phi\rangle \equiv \frac{1}{V_f}\int_{V_f}\Phi dV$ and $\boldsymbol{J}$ is a unit vector oriented along the velocity vector.

Energy equations [3–5]

Fluid phase:

$$(\rho c_p)_f\langle \boldsymbol{V}\rangle\cdot\nabla\langle T_f\rangle = \nabla(\lambda_{fe}\cdot\nabla\langle T_f\rangle) + h_{sf}\alpha_{sf}(\langle T_s\rangle - \langle T_f\rangle) \tag{5}$$

Solid phase:

$$0 = \nabla\cdot(\lambda_{se}\cdot\nabla\langle T_s\rangle - q_r) - h_{sf}\alpha_{sf}(\langle T_s\rangle - \langle T_f\rangle) \tag{6}$$

where the effective thermal conductivity for the fluid and solid phases are expressed as follows:

$$\lambda_{fe} = \varphi\lambda_f \tag{7}$$

$$\lambda_{se} = (1-\varphi)\lambda_s \tag{8}$$

and the specific surface area of the porous bed which appears in both of the energy equations is:

$$\frac{6(1-\varphi)}{d_p} \tag{9}$$

and the fluid-to-solid phase heat transfer coefficient in this study is based on the empirical correlation established by Wakao et al. [25], which can be presented as follows:

$$h_{sf} = \left(\frac{d_p\varphi}{0.2555Pr^{1/3}Re_d^{2/3}\lambda_f} + \frac{d_p}{10\lambda_s}\right)^{-1} \tag{10}$$

The extinction β, absorption κ and scattering σ_s coefficients are based on experimental data. Hsu et al. [26] presented a method of simultaneously obtaining the conductivity and extinction coefficients from the experimental data. The extinction coefficient can be presented as [7]:

$$\beta = \frac{\Psi}{d_p}(1-\varphi) \tag{11}$$

where the value of Ψ is constant and is based on the porous medium [14,15]. Mital et al. [27] also presented experimental data which shows that radiation properties is not sensitive to temperature in the range of 1200–1400 K. As such the absorption and scattering coefficients can be represented as:

$$\kappa = (2-\varepsilon)\frac{3}{2d_p}(1-\varphi) \tag{12}$$

$$\sigma_s = \varepsilon\frac{3}{2d_p}(1-\varphi) \tag{13}$$

2.2.2. Radiation transfer

With the assumption of collimated irradiation, a modified differential approximation (P-1 Model) is applied to address the problem here [28]. When the incident collimated irradiation is removed from the intensity field, the remnant intensity can deviate only slightly from the isotropic condition. Similar to the classic P-1 model we treat the remnant part as fairly diffuse, which is the result of emission from the boundary and within the medium, and also the radiation scattered away from the collimated irradiation, so we have to express the diffuse radiative flux q_d and the incident radiation G_d as follow:

$$\nabla q_d = \kappa\left(4\sigma\langle T_s\rangle^4 - G_d\right) + \sigma_s G_c \tag{14}$$

$$q_d = -\frac{1}{3\beta}\nabla G_d \tag{15}$$

combining the expressions for q_d and G_d, in Eqs. (14) and (15), the differential equation for G_d is obtained as:

$$0 = \frac{1}{3\beta}\nabla G_d^2 + \kappa\left(4\sigma\langle T_s\rangle^4 - G_d\right) + \sigma_s G_c \tag{16}$$

Meanwhile q_c, the remnant collimated radiative flux after partial extinction, by absorption and scattering, along its path in the direction which is perpendicular to the boundary is given by an exact solution as

$$q_c = G_c = q_0 e^{-\beta(H-y)} \tag{17}$$

2.2.3. Boundary conditions

B.C. 1: (Upper wall)

Considering the adiabatic boundary at the upper wall, the net heat flux including radiative and conductive heat flux for both the solid and fluid phases should be equal to zero:

$$\frac{1}{3\beta}\frac{\partial G_d}{\partial y}\bigg|_{y=H} + \lambda_{fe}\frac{\partial\langle T_f\rangle}{\partial y}\bigg|_{y=H} + \lambda_{se}\frac{\partial\langle T_s\rangle}{\partial y}\bigg|_{y=H} = 0 \tag{18}$$

while for the diffuse surface which connects with the solid matrix the radiative boundary condition can be expressed as:

$$-\frac{1}{3\beta}\frac{\partial G_d}{\partial y}\bigg|_{y=H} = \frac{1}{2(2-\varepsilon_1)}\varepsilon_1\left(4\sigma_s\langle T_w\rangle^4\big|_{y=H} - G_d|_{y=H}\right) \tag{19}$$

where ε_1 is the surface emittance of the upper wall.

Invoking the interface thermal parameter γ, the radiative flux $q_d|_{y=H}$ due to the diffuse flux from inside which points towards the upper wall is distributed between the solid and fluid phases as

$$\lambda_{fe}\frac{\partial\langle T_f\rangle}{\partial y}\bigg|_{y=H} = -\frac{\gamma}{3\beta}\frac{\partial G_d}{\partial y}\bigg|_{y=H} \tag{20}$$

$$\lambda_{se}\frac{\partial\langle T_s\rangle}{\partial y}\bigg|_{y=H} = -\frac{1-\gamma}{3\beta}\frac{\partial G_d}{\partial y}\bigg|_{y=H} \tag{21}$$

where the distribution parameter γ [29] can be defined as:

$$\gamma = \frac{\lambda_{fe}}{\lambda_{fe}+\lambda_{se}} \tag{22}$$

To consider the effect of radiation at the surface, in this work, we develop two models to describe the boundary conditions which are given below:

Model A:

When the thermal conductivity of the upper wall λ_w approaches a very large value, there will be local thermal equilibrium between the solid matrix and the wall:

$$\langle T_w\rangle|_{y=H} = \langle T_s\rangle|_{y=H} = \langle T_f\rangle|_{y=H} \tag{23}$$

Model B:

When the λ_w approaches zero, there will be local thermal non-equilibrium between the solid and fluid phases at the wall. To

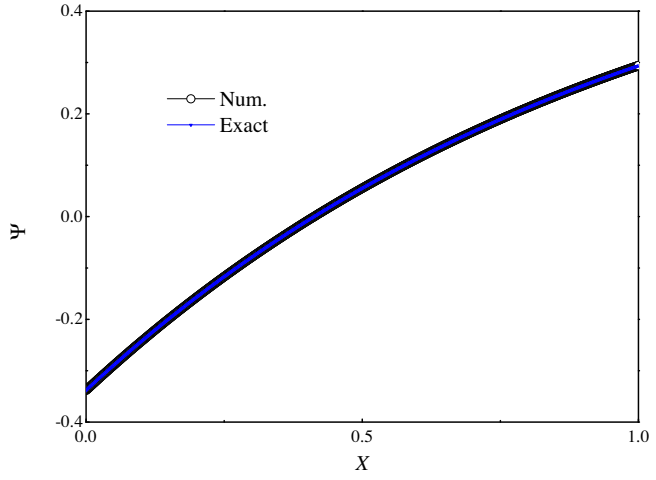

Fig. 2. Comparison of the numerical and exact solutions.

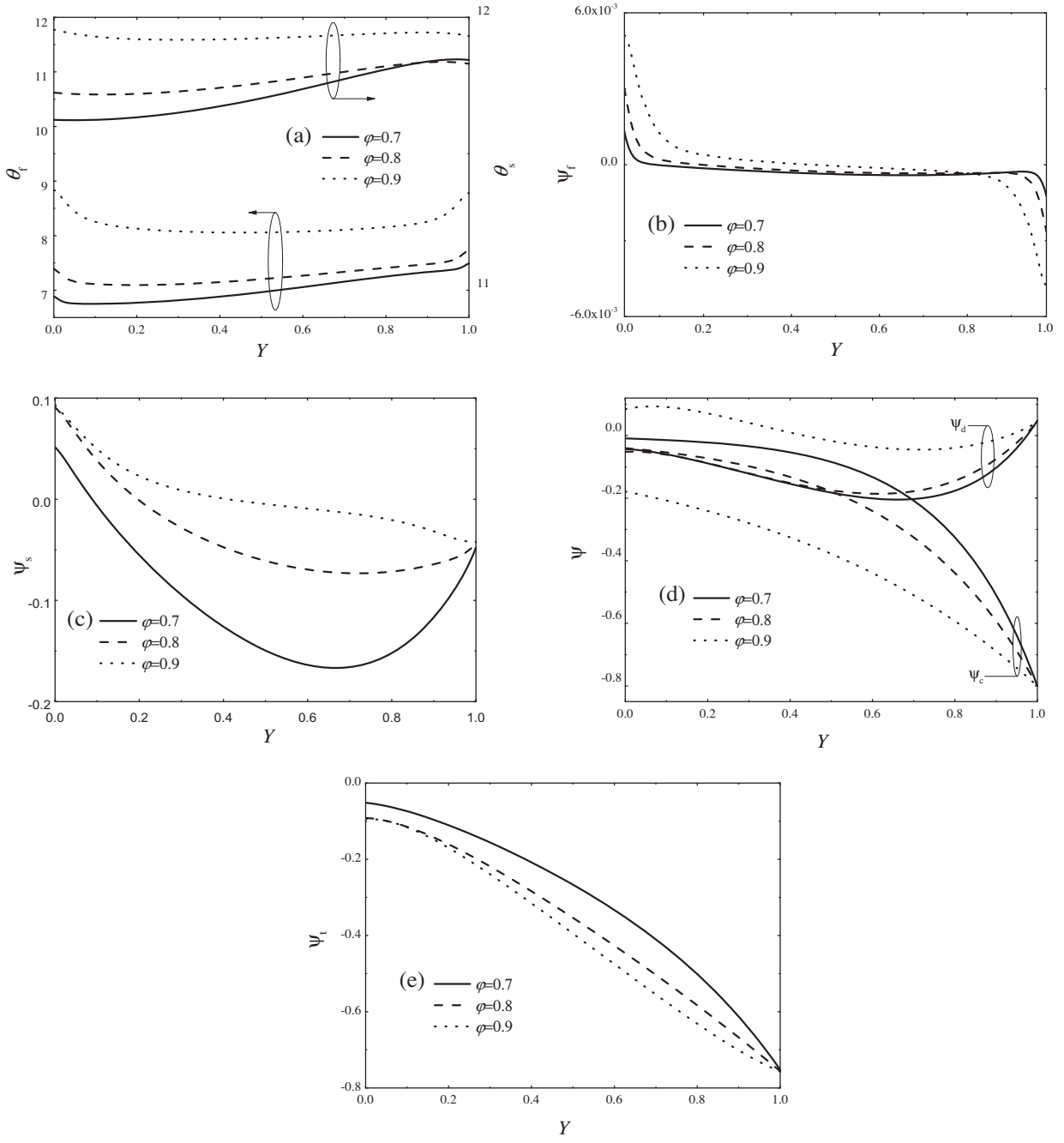

Fig. 3. Effect of the porosity φ on the temperature θ and heat flux Ψ distributions along the flow direction: (a) θ_s and θ_f; (b) Ψ_f; (c) Ψ_s; (d) Ψ_c and Ψ_d; (e) Ψ_t (d_p = 2 mm, Re_d = 500, q_0 = 1 MW).

obtain the temperature at the boundary local volume averaging method is applied as follows:

$$\langle T_w\rangle|_{y=H} = \varphi\langle T_f\rangle|_{y=H} + (1-\varphi)\langle T_s\rangle|_{y=H} \tag{24}$$

B.C. 2: (Bottom wall)

The ε_1 is the reflectance when considering the upper wall as a thin and transparent wall for the initial impinging heat flux q_0. The remnant part towards the inside is:

$$q_c|_{y=H} = (1-\varepsilon_1)q_0 \tag{25}$$

and the collimated radiative flux arriving at the bottom surface is H_c:

$$H_c|_{y=0} = e^{-\beta H} q_c|_{y=H} \tag{26}$$

Also for the adiabatic boundary condition under the impinging collimated irradiation, we have:

$$-H_c|_{y=0} + \frac{1}{3\beta}\frac{\partial G_d}{\partial y}\bigg|_{y=0} + \lambda_{fe}\frac{\partial\langle T_f\rangle}{\partial y}\bigg|_{y=0} + \lambda_{se}\frac{\partial\langle T_s\rangle}{\partial y}\bigg|_{y=0} = 0 \tag{27}$$

where the radiative boundary condition with collimated irradiation can be represented as:

$$-\frac{1}{3\beta}\frac{\partial G_d}{\partial y}\bigg|_{y=0} = \frac{1}{2(2-\varepsilon_2)}\left(\varepsilon_2\left(4\sigma_s\langle T_w\rangle^4\big|_{y=0} - G_d|_{y=0}\right) + 4(1-\varepsilon_2)H_c|_{y=0}\right) \tag{28}$$

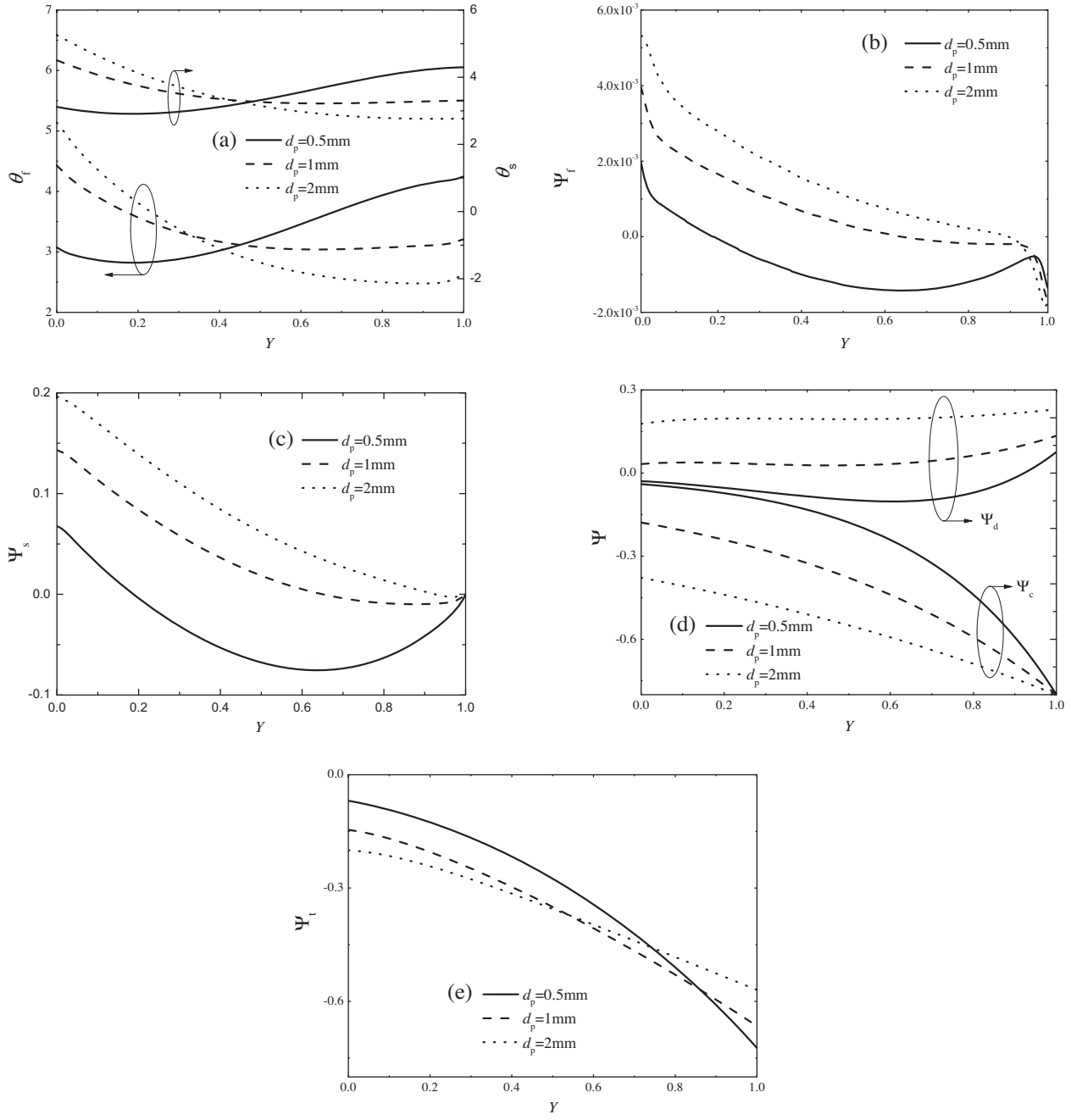

Fig. 4. Effect of the pore diameter d_p on the temperature θ and heat flux Ψ distributions along the Y direction. (a) θ_s and θ_f; (b) Ψ_f; (c) Ψ_s; (d) Ψ_c and Ψ_d; (e) Ψ_t (φ = 0.8, Re_d = 500, q_0 = 1 MW).

The diffuse radiative flux $q_d|_{y=0}$ from inside towards the boundary and the remnant collimated irradiation arriving at the bottom wall $H_c|_{y=0}$ will be distributed between the solid and fluid phases as

$$\lambda_{fe}\left.\frac{\partial\langle T_f\rangle}{\partial y}\right|_{y=0}=\gamma\left(-\frac{1}{3\beta}\left.\frac{\partial G_d}{\partial y}\right|_{y=0}-H_c|_{y=0}\right) \tag{29}$$

$$\lambda_{se}\left.\frac{\partial\langle T_s\rangle}{\partial y}\right|_{y=0}=(1-\gamma)\left(-\frac{1}{3\beta}\left.\frac{\partial G_d}{\partial y}\right|_{y=0}-H_c|_{y=0}\right) \tag{30}$$

similar to Eqs. (18), (19), temperature boundary conditions using models A and B can be defined as:

Model A:

$$\langle T_w\rangle|_{y=0}=\langle T_s\rangle|_{y=0} \tag{31}$$

Model B:

$$\langle T_w\rangle|_{y=0}=\varphi\langle T_f\rangle|_{y=0}+(1-\varphi)\langle T_s\rangle|_{y=0} \tag{32}$$

The related dimensionless parameters can be defined as follows:

$$Y=\frac{y}{H} \tag{33}$$

$$X=\frac{x}{L} \tag{34}$$

$$\theta_f=\frac{T_f}{T_e} \tag{35}$$

$$\theta_s=\frac{T_s}{T_e} \tag{36}$$

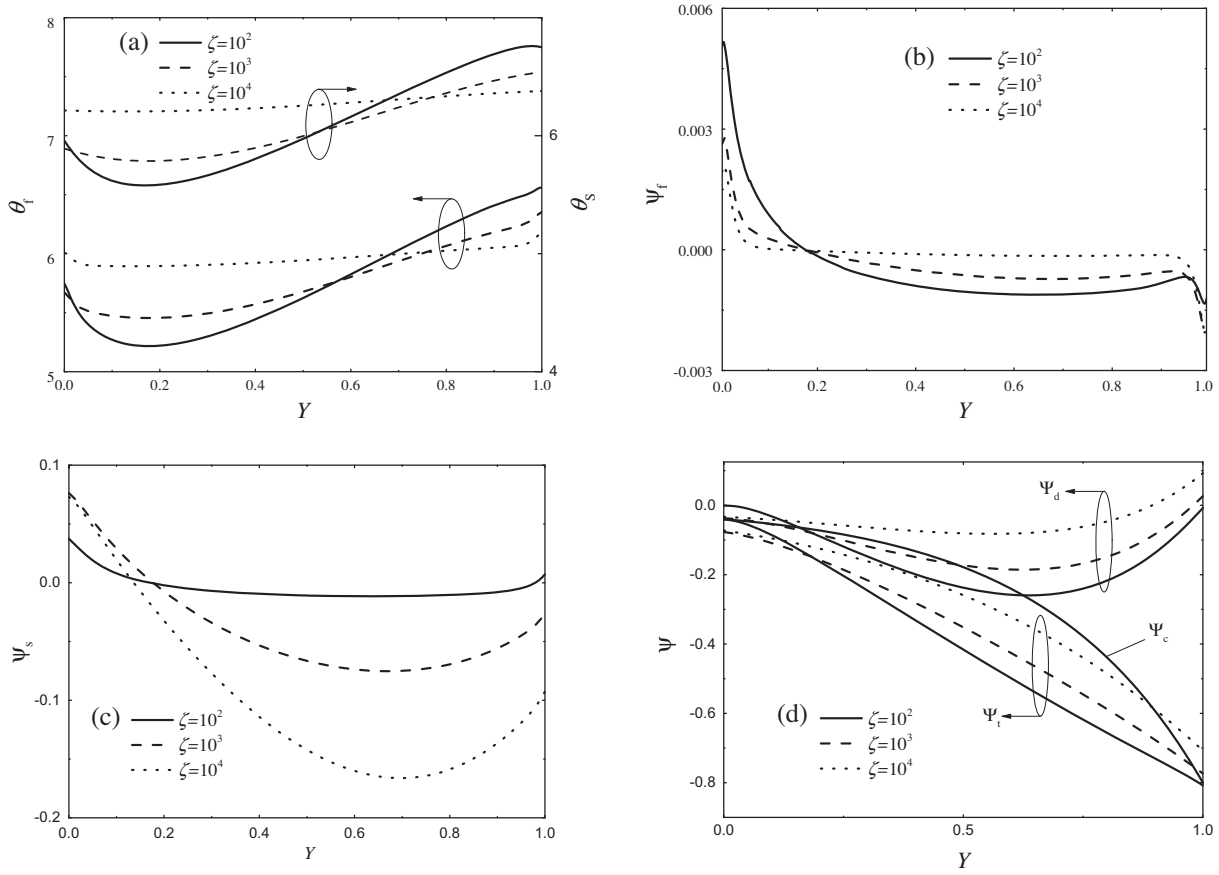

Fig. 5. Effect of the ratio of thermal conductivities ζ on the temperature θ and heat flux Ψ distributions along the Y direction. (a) θ_s and θ_f; (b) Ψ_f; (c) Ψ_s; (d) Ψ_c and Ψ_d; (e) Ψ_t (φ = 0.8, d_p = 2 mm, Re_d = 500, q_0 = 1 MW).

where the H and L are the height and the length of the channel, and T_e = 300 K is the ambient temperature. The conductive heat flux for the solid phase Ψ_s and the fluid phase, Ψ_f, can be represented as

$$\Psi_s = -\frac{\lambda_{se}}{q_0}\frac{\partial T_s}{\partial y} \tag{37}$$

$$\Psi_f = -\frac{\lambda_{fe}}{q_0}\frac{\partial T_f}{\partial y} \tag{38}$$

and the diffuse radiative flux Ψ_d, the collimated radiative flux, Ψ_c, and the total radiative flux, Ψ_t, can be represented as

$$\Psi_d = -\frac{1}{3\beta q_0}\frac{\partial G_d}{\partial y} \tag{39}$$

$$\Psi_c = \frac{G_c}{q_0} \tag{40}$$

$$\Psi_t = \frac{q_d + q_c}{q_0} \tag{41}$$

3. Numerical procedure

The governing equations are discretized using a SIMPLE algorithm and the 2nd order upwind differencing method is employed to discretize the convective terms. The convergence is considered to have been reached when the relative variation of temperature between consecutive iterations is smaller than 10^{-8} for all the grid points in the computational domain after the grid independent test. To further validate our results especially the radiation transfer using the P-1 approximation, the results will be compared with the exact solution considering a plane-parallel slab of an absorbing and isotropically scattering medium with a black cold bottom surface which has no effect on convection in the channel area as shown in Fig. 1. For simplicity, the single scattering albedo ω is set to unity. Fig. 2 displays the very good agreement between our numerical result and the exact solution for the diffusive radiation heat flux which can be presented as:

$$q_d = \left(\frac{5 - e^{-\tau_H}}{4 + 3e^{-\tau_H}} - e^{-\tau}\right) \tag{42}$$

where the τ_H is the optical thickness at the position y = 0.

4. Results and discussion

4.1. Effect of Porosity φ, Pore diameter d_p, and ratio of solid to fluid thermal conductivity ζ

In what follows, we have based our analysis on model A. Fig. 3 depicts the dimensionless temperature distribution θ and heat flux Ψ for different porosities with constant pore diameter d_p, pore Reynolds number Re_d, ratio of solid to fluid thermal conductivity ζ, and initial incident radiative flux q_s. It can be seen that both the solid and fluid temperatures near the upper wall are always slightly larger than that at the bottom one.

The temperature θ_s along the Y direction for the solid phase generally decreases in the incident direction; however, the fluid phase temperature θ_f at the boundary is always higher than that in the middle area. The conductive heat flux for the fluid phase Ψ_f is negligible compared with that for the solid phase Ψ_s. It can

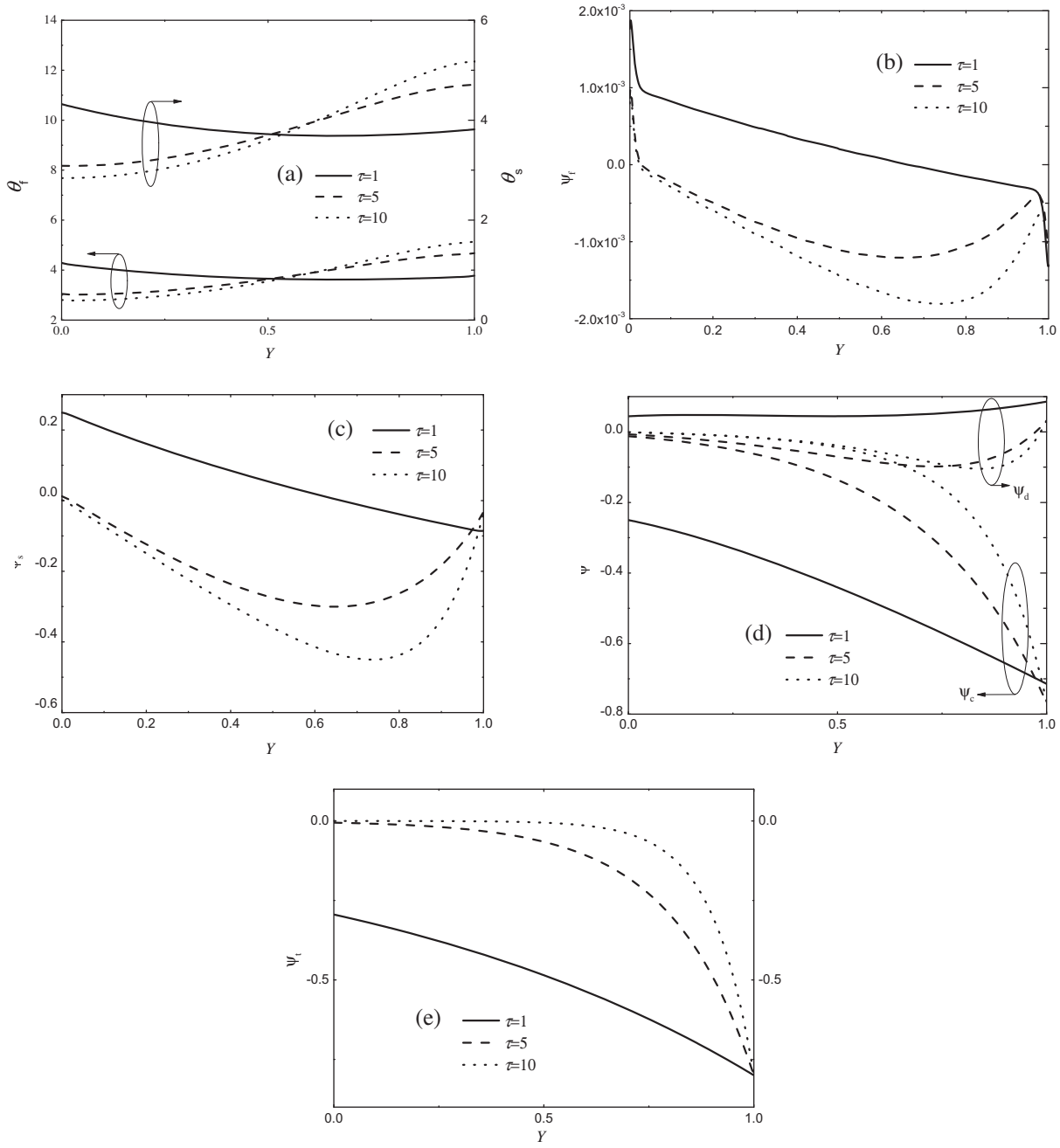

Fig. 6. Effect of the optical thickness τ on the temperature θ and the heat flux Ψ distributions along the Y direction. (a) θ_s and θ_f; (b) Ψ_f; (c) Ψ_s; (d) Ψ_c and Ψ_d; (e) Ψ_t ($\varphi = 0.8$, $d_p = 1$ mm, $Re_d = 500$, $q_0 = 1$ MW).

also be seen that its absolute peak value decreases in the boundary layer from the wall to the inner area (Fig. 3(b) and (c)), and in the negative direction, it increases first from the upper wall ($Y = 1$) then decreases to zero while it grows as it approaches the bottom wall ($Y = 0$).

Fig. 3(d) and (e) shows that both the absolute value of collimated radiative flux Ψ_c and total radiative flux Ψ_t increase along the Y direction. Comparing the diffuse and total radiative flux distributions in Fig. 3(e), it can also be seen that Ψ_c dominates the radiation transfer. A maximum absolute value point also appears on the distribution of the diffuse radiative flux Ψ_d at the center of the Y direction which is similar to the distribution of the conductive heat flux for the solid phase. This is because its distribution is dependent on the optical thickness, τ of the solid.

As expected in Fig. 3(b) and (c), the extinction coefficient β decreases with an increase in porosity φ, resulting in more collimated radiative flux Ψ_c arriving at the bottom wall, consequently, both the conductive heat flux for solid and fluid (Ψ_s and Ψ_f) at the bottom wall increases with an increase in the porosity φ.

The higher the porosity, the sparser the pore structure will be, hence the extinction coefficient β decreases with an increase in the porosity φ. On the other hand, a decrease in porosity φ, results in a decrease in the absolute value of the diffusive radiative flux Ψ_d i.e. a decrease in the diffuse effect, while, for the collimated part Ψ_c, the reverse trend is observed (Fig. 3(d) and (e)), which shows the restricted relationship between the diffusive and collimated radiative flux.

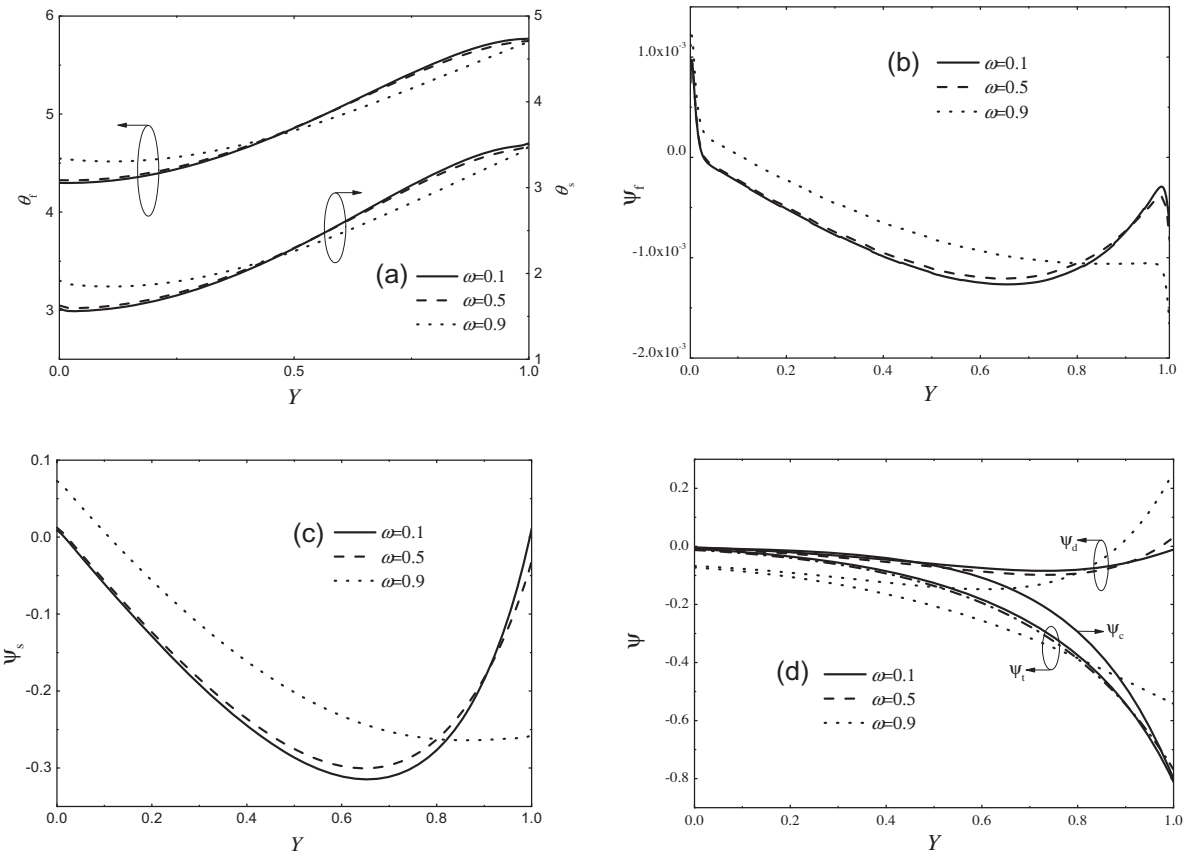

Fig. 7. Effect of the scattering albedo ω on the temperature θ and heat flux Ψ distributions along the Y direction. (a) θ_s and θ_f; (b) Ψ_f; (c) Ψ_s ($\varphi = 0.8$, $d_p = 1$ mm, $Re_d = 500$, $q_0 = 1$ MW).

Fig. 4 shows the effect of d_p on the distribution of the temperature θ and the heat flux Ψ along the Y direction when $\varphi = 0.8$, $Re_d = 500$, $q_0 = 1$ MW. As can be seen in Fig. 4(a), with an increase in d_p, the temperature increases at the bottom wall while it decreases at the upper wall for both the solid and fluid phases (θ_f and θ_s). The corresponding conductive heat flux for both the solid and fluid phases (Ψ_f and Ψ_s) increases sharply at the bottom wall while it decreases at the upper wall. The reason is that a larger pore diameter enhances the incident collimated radiative flux transfer from the boundary inwards as seen by the distributions of Ψ_c and Ψ_d in Fig. 4(d); that is larger d_p leads to a larger difference between Ψ_c and Ψ_d. Furthermore, as can be seen in Fig. 4(e), the gradient of total radiative flux Ψ_t decreases with an increase in d_p due to the enhanced radiation transfer in the incident direction.

The effect of the ratio of solid to fluid thermal conductivities ζ on the distribution of the temperature θ and heat flux Ψ along the Y direction when $\varphi = 0.8$, $d_p = 1$ mm, $Re_d = 500$, $q_0 = 1$ MW are displayed in Fig. 5. As can be seen, the distribution of the temperature θ for both of the solid and fluid phases along the Y direction becomes smoother with an increase in ζ. It also can be seen that, the heat flux at the boundary increases for solid phase but decreases sharply for the fluid phase. As expected, the collimated radiation Ψ_c is constant with a change in ζ due to the constant porosity φ and pore diameter d_p (Fig. 4(d)), but the absolute peak values for Ψ_d and Ψ_t decrease substantially with an increase in ζ, which is opposite to the effect that ζ has on Ψ_s. This phenomenon shows the relationship between the conductive and radiative heat transfer in the Y direction.

4.2. Effect of the optical thickness τ, the single scattering albedo ω and the emittance of the boundary wall ε_w

To analyze the radiation transfer process considering the actual properties of the porous media the optical thickness τ is chosen as a parameter from 1 to 10. τ can be defined as follows:

$$\tau = \beta H \tag{43}$$

$$\beta = \kappa + \sigma_s \tag{44}$$

The effect of optical thickness τ on the dimensionless temperature distribution θ and heat flux Ψ along the Y direction is displayed in Fig. 6. It shows that when τ increases, the temperature at the bottom wall decreases while it increases slightly at the upper wall. When τ is small ($\tau = 1$), the temperature at the upper wall is lower than that at the bottom. The variation of these parameters changes the distribution of the collimated radiation in the porous medium, leading to a change in the distribution of heat source for the solid phase.

For the large optical thicknesses ($\tau = 5$, $\tau = 10$) collimated, diffuse and total radiative flux all converge to 0 which shows that the attenuation of radiative energy transfer in the Y direction is weakened as can be seen in the Fig. 6(d) and (e). The effect of single scattering albedo ω on the temperature distribution θ and heat flux Ψ is also displayed in Fig. 7. Here the single scattering albedo ω represents the percentage of the diffuse part and can be defined as follows:

$$\omega = \frac{\sigma_s}{\beta} \tag{45}$$

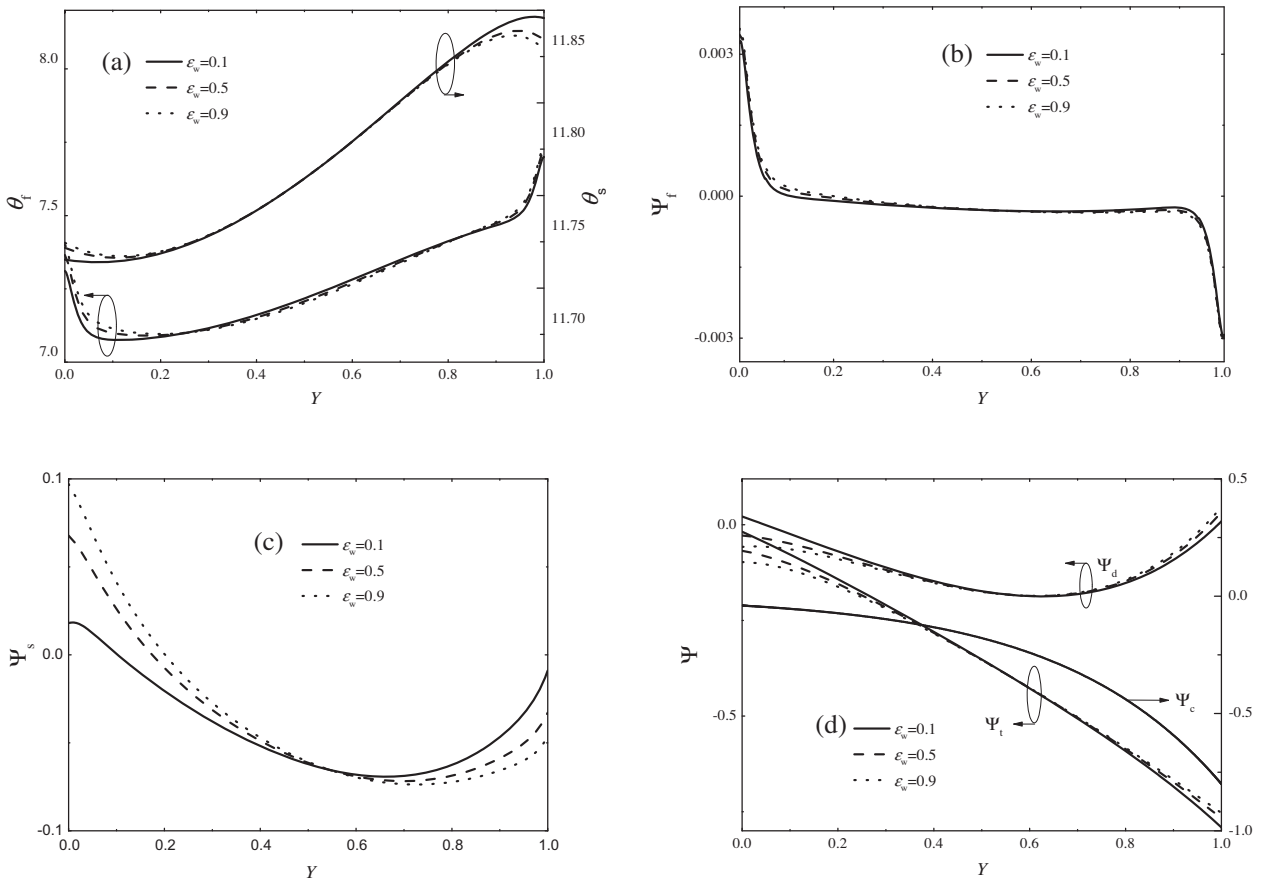

Fig. 8. Effect of emittance ε_w on the temperature θ and heat flux Ψ distributions along the Y direction. (a) θ_s and θ_f; (b) Ψ_f; (c) Ψ_s; (d) Ψ_c, Ψ_d and Ψ_t (φ = 0.8, d_p = 1 mm, Re_d = 500, q_0 = 1 MW).

where σ_s is the scattering coefficient of the porous medium. As can be seen the larger ω leads to a lower temperature gradient. As expected, the collimated radiative flux Ψ_c is constant with a change in ω, as shown in Fig. 7(d), but, in the same figure, the distribution of the diffuse radiative flux Ψ_d along the Y direction is sensitive to the change of scattering albedo ω. For the smaller ω (ω = 0.1, ω = 0.5), the distribution of Ψ_d is more subtle than that for the larger one along the incident direction from the upper wall to the bottom one, which directly shows that the increase in ω will increase the proportion of the radiative flux in the total energy transfer process in the Y direction. Fig. 8 depicts the effect of the boundary wall emittance ε_w on the distribution of temperature θ and heat flux Ψ along the Y direction. For the comparison purposes, each of the wall emittances was set to ε_w. As can be seen the influence of ε_w on the solid phase temperature field always appears on the region near the boundary wall, but its effect on the fluid temperature is relatively negligible. The conductive heat flux increases with an increase in ε_w at the wall. For the distribution of the radiative flux, it is shown that the larger ε_w, the larger the absolute value of diffuse radiative flux Ψ_d will be. However, the reverse trend is observed for the solid phase's conductive heat flux that is a larger ε_w enhances the radiative transfer at the boundary.

4.3. Effect of coupled thermal boundary conditions

As mentioned earlier, models A and B provide two different limiting boundary conditions under LTNE condition coupled with radiation transfer expressed by Eqs. (20) and (21) respectively. The effect of different porosity φ, ratio of solid to fluid thermal conductivity ζ and pore Reynolds number Re_d on these two models is presented in Figs. 9–12. It can be seen that the temperature near the wall for model B is always higher than that for model A for both the solid and fluid phases. Similarly, the effects on the diffusive or total radiative flux (Ψ_d, Ψ_t) distribution along the Y direction between the two models can be seen in Figs. 9–12. Figs. 9 and 10 demonstrated that as the ratio of solid to fluid thermal conductivities ζ increases from 10^2 to 10^3, the heat flux distribution parameter γ decreases resulting in an increase in the heat flux difference between the solid and fluid phases.

4.4. Nusselt number

To analyze the energy transport at the upper wall the Nusselt number Nu is defined as follows:

$$Nu = \frac{H}{T_{f,w} - T_{f,m}} \frac{\partial T_f}{\partial y} \tag{46}$$

where $\partial T_f/\partial y$ is the temperature gradient at the upper wall, $T_{f,w}$ the fluid temperature at the upper wall and $T_{f,m}$ is the mean temperature across the section in the Y direction defined as:

$$T_{f,m} = \frac{\int_0^H u T_f dy}{U_0 H} \tag{47}$$

Fig. 13 displays the effect of porosity φ and pore diameter d_p on Nu. As it can be seen for a constant d_p, Nu increases as φ increases due to an increase in the temperature gradient $\partial T_f/\partial y|_{y=H}$. Similarly, for a constant φ, Nu increases with an increase in d_p. The above trends demonstrate that an increase in porosity φ and pore diameter d_p enhances the transfer of radiative energy.

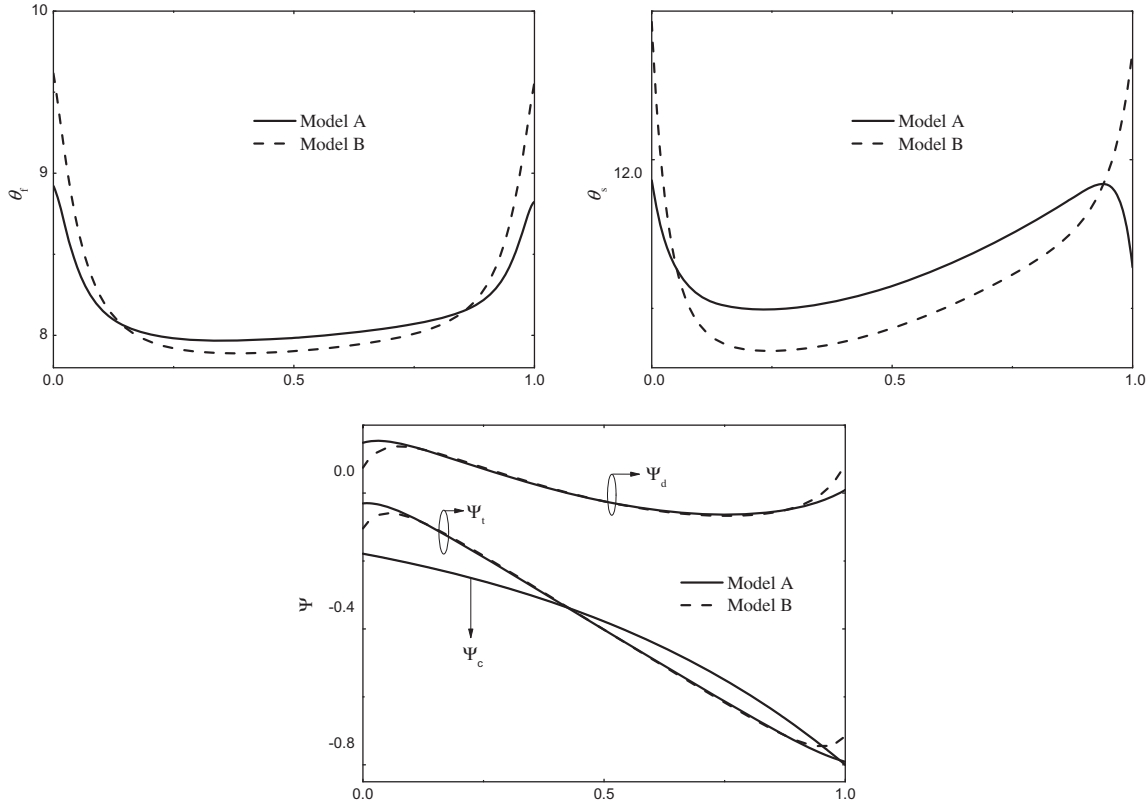

Fig. 9. Effect of the porosity φ, ζ and Re_d on Model A and B ($\varphi = 0.9$, $Re_d = 500$, $\zeta = 100$).

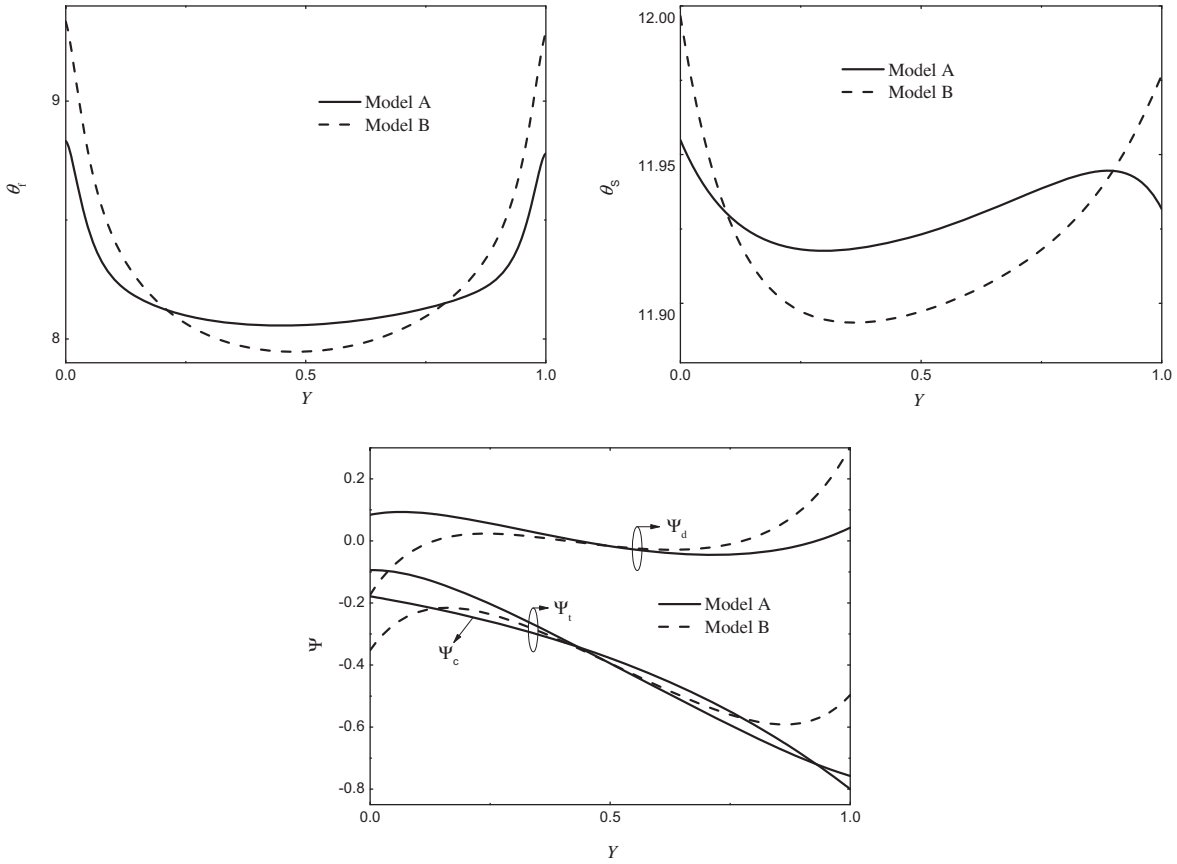

Fig. 10. Effect of the porosity φ, ζ and Re_d on Model A and B ($\varphi = 0.9$, $Re_d = 500$, $\zeta = 1000$).

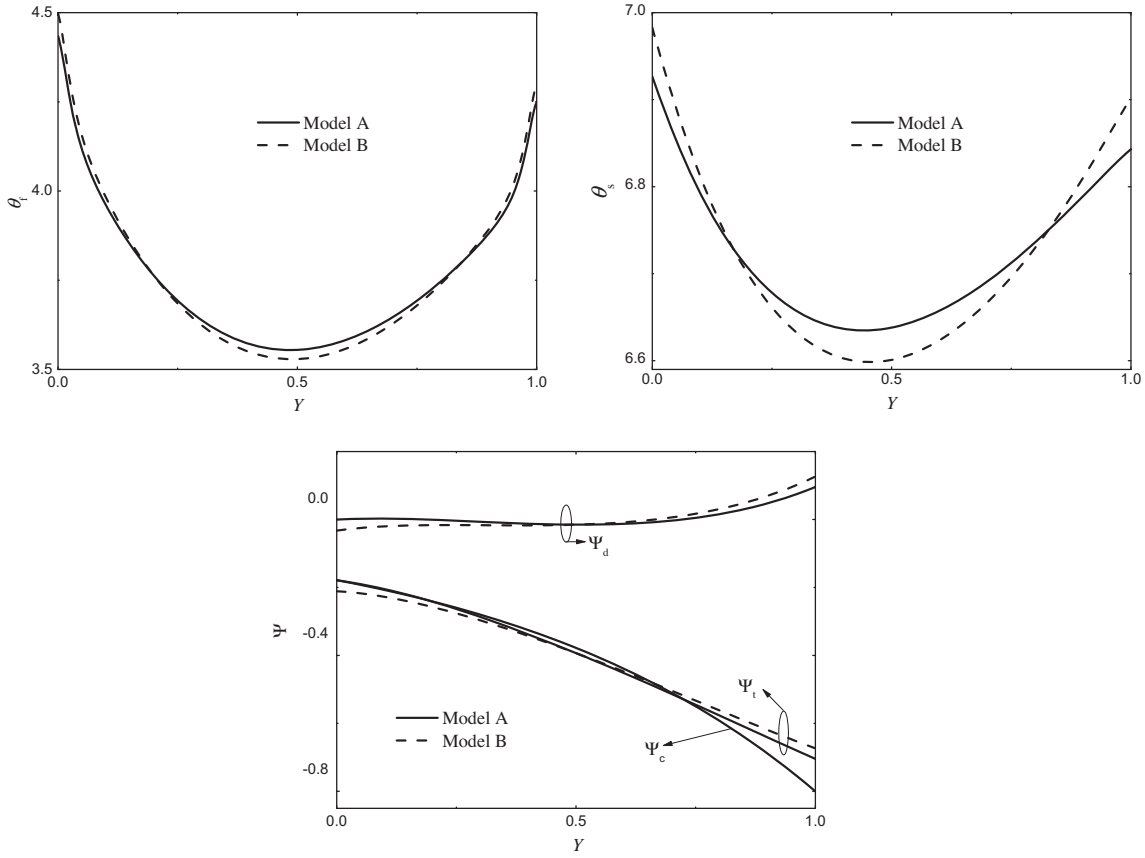

Fig. 11. Effect of the porosity φ, ζ and Re_d on Model A and B ($\varphi = 0.9$, $Re_d = 1000$, $\zeta = 1000$).

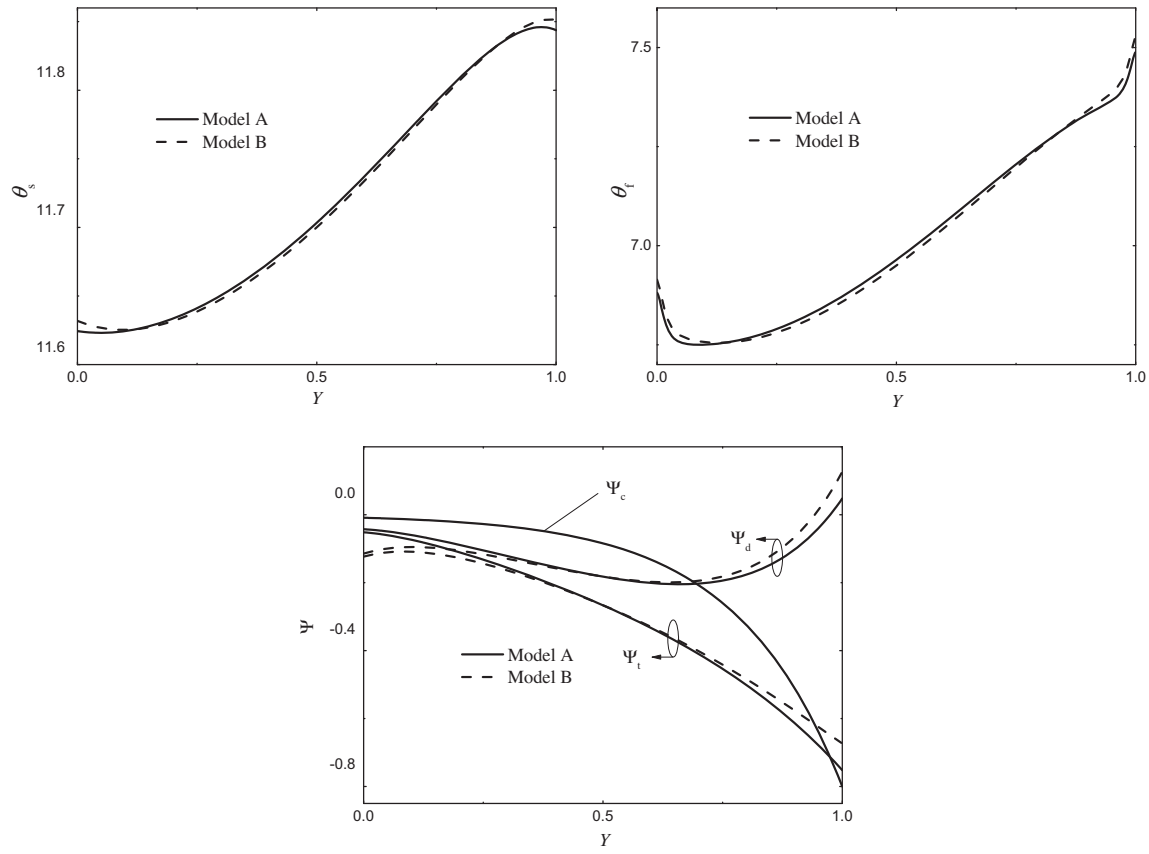

Fig. 12. Effect of the porosity φ, ζ and Re_d on Model A and B ($\varphi = 0.7$, $Re_d = 500$, $\zeta = 100$).

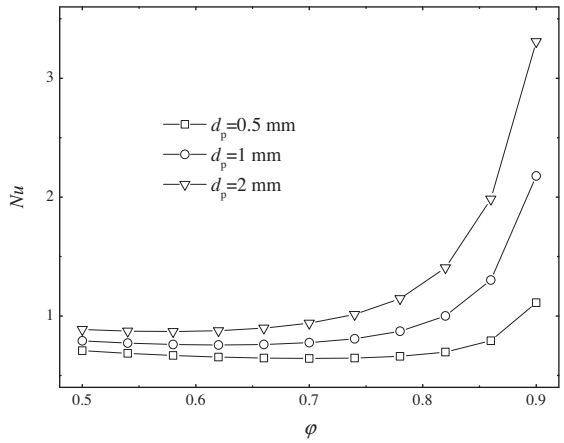

Fig. 13. Effect of the porosity φ and pore diameter d_p on the Nusselt number, Nu ($Re_d = 500$, $q_0 = 1$ MW).

5. Conclusions

Convective and radiative transport in porous media in the presence of collimated irradiation and local thermal non-equilibrium is analyzed in this work. A modified P-1 approximation with collimated irradiation was introduced to incorporate the radiative transfer. Two boundary condition models incorporating the LTNE condition were constructed and analyzed. The following conclusions can be drawn based on our analysis.

(1) An increase in the porosity φ leads to a sparser pore structure and a smaller extinction coefficient β, resulting in an increase in the radiative flux arriving at the bottom wall. Consequently, the heat flux for both the solid and fluid phases (Ψ_s and Ψ_f) at the bottom wall increases with an increase in the porosity. The absolute value of both the collimated and the total radiative fluxes along the Y direction increase with an increase in φ. However, for the diffuse part Ψ_d, the reverse trend is observed.

(2) The temperature increases at the bottom wall with an increase in the pore diameter d_p, but it decreases at the upper wall for both the solid and fluid phases; while, the corresponding conductive heat flux for both the solid and fluid phases (Ψ_f and Ψ_s) increases sharply at the bottom wall. This is due to the enhanced radiation energy transfer from the boundary for the larger pores.

(3) The heat flux distribution parameter γ decreases with an increase in the ratio of solid to fluid thermal conductivity ζ. The collimated radiation Ψ_c remains constant when ζ varies, but the absolute peak values for both Ψ_d and Ψ_t increase substantially with an increase in ζ. An opposite trend is observed for Ψ_f and Ψ_s. This phenomenon displays the relationship between the conductive and radiative heat transfer in the Y direction.

(4) The radiative flux at the bottom wall decreases with an increase in the optical thickness τ resulting in a decrease in the temperature at the bottom wall and an increase at the upper wall. The mechanism for this behavior is similar to the effect of porosity φ and pore diameter d_p, that is a variation in τ changes the distribution of collimated radiation leading to a change in the heat source distribution for the solid phase.

(5) Larger scattering albedo ω leads to a lower temperature gradient for both the solid and fluid phases. An increase in ω increases the diffusive portion in the total radiative transfer process in the incident direction.

(6) The influence of the wall emittance ε_w on the temperature and heat flux fields always appears in a region near the boundary. As ε_w increases, the absolute value of diffuse radiative flux Ψ_d increases. However, the reverse trend is found for the conductive heat flux for both the solid and fluid phases as ε_w increases.

(7) The solid and fluid phase temperatures near the wall are higher for model B as compared to model A. The radiative flux Ψ_d and Ψ_t using model B are smaller compared to those obtained when using model A near the bottom wall, but larger at the upper wall. An increase in Re_d results in a decrease in the radiative contribution, hence, the difference between model A and B results decreases for Ψ_d and Ψ_t.

(8) Nu increases with an increase in φ at a constant d_p, due to an increase in the temperature gradient. Similarly, at a constant φ, Nu increases with an increase in d_p. This trend demonstrates that an increase in porosity, φ and the pore diameter, d_p enhances the transfer of radiative energy.

Conflict of interest

None declared.

Acknowledgments

The support of the National Basic Research Program (973 Program) and National High Technology Research and Development Program (863 Program) of Chinese Science and Technology Department under Project Numbers 2010CB227102 and 2007AA05Z445 as well as the grant by the Chinese Scholarship Council and the Fundamental Research Fund for Central Universities (2014B34514) are acknowledged.

References

[1] K. Vafai, Handbook of Porous Media, CRC, New York, 2000.
[2] K. Vafai, Convective flow and heat transfer in variable-porosity media, J. Fluid Mech. 147 (1984) 233–259.
[3] K. Vafai, M. Sozen, Analysis of energy and momentum transport for fluid flow through a porous bed, J. Heat Transfer 112 (3) (1990) 690–699.
[4] B. Alazmi, K. Vafai, Analysis of variants within the porous media transport models, J. Heat Transfer 122 (2000) 303–326.
[5] K. Yang, K. Vafai, Analysis of temperature gradient bifurcation in porous media – an exact solution, Int. J. Heat Mass Transfer 53 (19–20) (2010) 4316–4325.
[6] K. Yang, K. Vafai, Analysis of heat flux bifurcation inside porous media incorporating inertial and dispersion effects – an exact solution, Int. J. Heat Mass Transfer 54 (25–26) (2011) 5286–5297.
[7] C.L. Tien, Thermal-radiation in packed and fluidized-beds, J. Heat Transfer 110 (4B) (1988) 1230–1242.
[8] C.L. Tien, K. Vafai, Convective and radiative heat transfer in porous media, Adv. Appl. Mech. 27 (1990) 225–281.
[9] K. Vafai, J. Ettefagh, Analysis of the radiative and conductive heat transfer characteristics of a waste package canister, J. Heat Transfer 110 (1988) 1011–1014.
[10] B.P. Singh, M. Kaviany, Independent theory versus direct simulation of radiation heat transfer in packed beds, Int. J. Heat Mass Transfer 34 (11) (1991) 2869–2882.
[11] B.P. Singh, M. Kaviany, Modelling radiative heat transfer in packed beds, Int. J. Heat Mass Transfer 35 (6) (1992) 1397–1405.
[12] C.Y. Zhao, T.J. Lu, H.P. Hodson, Thermal radiation in ultralight metal foams with open cells, Int. J. Heat Mass Transfer 47 (14–16) (2004) 2927–2939.
[13] C.Y. Zhao, S.A. Tassou, T.J. Lu, Analytical considerations of thermal radiation in cellular metal foams with open cells, Int. J. Heat Mass Transfer 51 (3–4) (2008) 929–940.
[14] T.J. Hendricks, J.R. Howell, New radiative analysis approach for reticulated porous ceramics using discrete ordinates method, J. Heat Transfer 118 (4) (1996) 911–917.
[15] T.J. Hendricks, J.R. Howell, Absorption/scattering coefficients and scattering phase functions in reticulated porous ceramics, J. Heat Transfer 118 (1) (1996) 79–87.
[16] D. Baillis, M. Raynaud, J.F. Sacadura, Spectral radiative properties of open-cell foam insulation, J. Thermophys. Heat Transfer 13 (3) (1999) 292–298.
[17] D. Baillis, J.-F. Sacadura, Thermal radiation properties of dispersed media: theoretical prediction and experimental characterization, J. Quant. Spectrosc. Radiat. Transfer 67 (5) (2000) 327–363.

[18] P. Wang, K. Vafai, D.Y. Liu, Analysis of radiative effect under local thermal non-equilibrium conditions in porous media-application to a solar air receiver, Numer. Heat Transfer, Part A: Appl. 65 (2014) 931–948.
[19] G. Flamant, G. Olalde, High temperature solar gas heating comparison between packed and fluidized bed receivers – I, Sol. Energy 31 (5) (1983) 463–471.
[20] R.D. Skocypec, R.F. Boehm, J.M. Chavez, Heat transfer modeling of the IEA/SSPS volumetric receiver, J. Sol. Energy Eng. 111 (2) (1989) 138–143.
[21] J.M. Chavez, C. Chaza, Testing of a porous ceramic absorber for a volumetric air receiver, Sol. Energy Mater. 24 (1–4) (1991) 172–181.
[22] F. Bai, One dimensional thermal analysis of silicon carbide ceramic foam used for solar air receiver, Int. J. Therm. Sci. 49 (12) (2010) 2400–2404.
[23] C. Xu, Z. Song, L.-D. Chen, Y. Zhen, Numerical investigation on porous media heat transfer in a solar tower receiver, Renewable Energy 36 (3) (2011) 1138–1144.
[24] Z.Y. Wu, C. Caliot, G. Flamant, Z.F. Wang, Coupled radiation and flow modeling in ceramic foam volumetric solar air receivers, Sol. Energy 85 (9) (2011) 2374–2385.
[25] N. Wakao, T. Funazkri, Effect of fluid dispersion coefficients on particle-to-fluid mass transfer coefficients in packed beds: correlation of Sherwood numbers, Chem. Eng. Sci. 33 (10) (1978) 1375–1384.
[26] P.-F. Hsu, J.R. Howell, Measurement of thermal conductivity and optical properties of porous partially stabilized zirconia, Exp. Heat Transfer 5 (4) (1992) 293–313.
[27] R. Mital, J.P. Gore, R. Viskanta, Measurements of radiative properties of cellular ceramics at high temperatures, J. Thermophys. Heat Transfer 10 (1) (1996) 33–38.
[28] K. Yang, K. Vafai, Restrictions on the validity of the thermal conditions at the porous-fluid interface – an exact solution, J. Heat Transfer 133 (11) (2011) 112601.
[29] M. Becker, S. Cordes, M. Bohmer, The development of open volumetric receivers, in: Proc. of Sixth Int. Symp. on Solar Thermal Concentrating Technologies, 1992, pp. 945–952.